

# Effects of a Mixed O/F Ligand in the Tavorite-Type $\text{LiVPO}_4\text{O}$ Structure

Sorour Semsari Parapari,<sup>†,‡</sup> Jean-Marcel Ateba Mba,<sup>†</sup> Elena Tchernychova,<sup>†</sup> Gregor Mali,<sup>†</sup> Iztok Arčon,<sup>§,||</sup> Gregor Kapun,<sup>†</sup> Mehmet Ali Gülgün,<sup>‡</sup> and Robert Dominko<sup>\*,†,⊥,#</sup>

<sup>†</sup>National Institute of Chemistry, Hajdrihova 19, 1000 Ljubljana, Slovenia

<sup>‡</sup>Sabancı University, Tuzla 34956, Istanbul, Turkey

<sup>§</sup>University of Nova Gorica, Vipavska 13, 5000 Nova Gorica, Slovenia

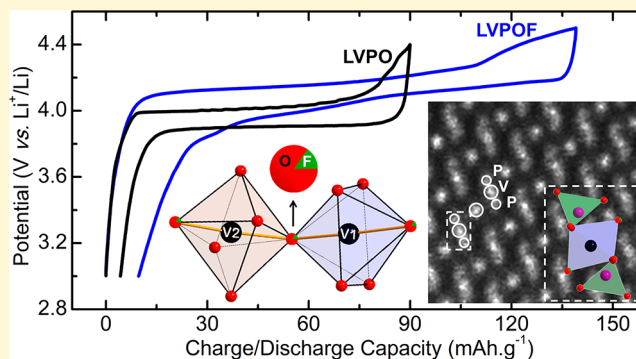
<sup>||</sup>Institute Jožef Stefan, Jamova 39, 1000 Ljubljana, Slovenia

<sup>⊥</sup>University of Ljubljana, Večna pot 117, SI-1000 Ljubljana, Slovenia

<sup>#</sup>ALISTORE-ERI, FR3104, 80039 Amiens cedex, France

## Supporting Information

**ABSTRACT:** We report the synthesis and detailed structural and chemical characterization including electrochemical properties of a lithium vanadium oxy/fluoro-phosphate material. To the best of our knowledge, we have for the first time synthesized a  $\text{LiVPO}_4\text{O}$ -type phase with a mixed O/F ligand. In the synthesis procedure, the  $\text{LiVPO}_4\text{O}$  precursor compound was fluorinated via LiF incorporation, with preservation of the  $\text{LiVPO}_4\text{O}$  framework structure. The operating potential of the synthesized material is increased compared to that of the  $\text{LiVPO}_4\text{O}$  precursor (4.12 V vs 3.95 V versus metallic lithium, respectively). The related increase in operating potential was assigned to the effect of the intermixing O/F ligand, which is attained via the successful fluorine incorporation into the  $\text{LiVPO}_4\text{O}$  structure. A characterization of the investigated materials was performed using microscale-covering XRD, XANES, and NMR techniques as well as nanoscale spatially resolved imaging and analytical STEM techniques. The obtained oxy/fluoro-phosphate phase is isostructural to  $\text{LiVPO}_4\text{O}$ ; however, the presence of the mixed O/F ligand promoted a higher symmetry of vanadium octahedra. These variations of the vanadium local environment along with the observed inhomogeneous distribution of the incorporated fluorine gave rise to the minor local deviations in vanadium valence. Our results clearly emphasize the connection among the fluorine ligand incorporation, its local distribution, and the electrochemical properties of the material.



## 1. INTRODUCTION

The requirement for sustainable, high specific energy density materials for the next generations of Li-ion batteries is a driving force for the continuous development of novel materials with improved properties. One of the demands is a stable crystal structure that allows for extraction/insertion of the  $\text{Li}^+$  ions, which is supported by the redox centers, preferably within transition metals. Among other candidates, a three-dimensional framework built of transition metals and polyanions  $(\text{XO}_4)^{n-}$ , e.g.,  $\text{LiFePO}_4$ , represent attractive materials with improved inherent safety. Another representative of this class, Tavorite compounds ( $\text{LiMXO}_4\text{Y}$ ), allows for adjustment of the working potential via using different transition metals as well as tuning the inductive effect of the polyanion and the bridging anion (ligand), i.e., O, F, and OH. Thus, the potential of the redox couple is highly influenced by the local environment of the transition metal.<sup>1–4</sup> Among the Tavorite compounds, vanadium-based phosphates  $\text{LiVPO}_4\text{O}$  and  $\text{LiVPO}_4\text{F}$  are the most

appealing ones because of their attractive electrochemical properties. Indeed, the redox couple in  $\text{LiVPO}_4\text{O}$  ( $\text{V}^{+4}/\text{V}^{+5}$ ) operates at 3.95 V, whereas in  $\text{LiVPO}_4\text{F}$  the redox couple ( $\text{V}^{+3}/\text{V}^{+4}$ ) operates at 4.26 V vs Li.<sup>5–10</sup> Fluorinated compounds have been shown to possess better electrochemical performance as well as safety parameters. They generally have a higher redox potential and more stable host lattice due to the high electronegativity of the  $\text{F}^-$  anion, which could play a role in the stabilization of the structure. The inductive effect of fluorine prompts the formation of a more ionic metal–ligand bond. This, in its turn, leads to a lower energy of the antibonding orbital level and, thus, to a higher potential difference vs Li.<sup>11</sup> In addition, the crystal structure strongly influences the key electrochemical properties in these systems.<sup>1</sup>

Received: September 11, 2019

Revised: December 8, 2019

Published: December 9, 2019

Recently studied lithium vanadium oxy/fluoro-phosphate compounds demonstrated oxygen partial substitution by fluorine<sup>12–17</sup> so as to form a solid solution. Such compounds were produced either by solid-state synthesis or by oxidation of the LiVPO<sub>4</sub>F-based compound. In these works, promising results were achieved where the produced materials were distinguishable from LiVPO<sub>4</sub>F and LiVPO<sub>4</sub>O. Kim et al.<sup>12</sup> synthesized the LiVPO<sub>4</sub>O<sub>0.75</sub>F<sub>0.25</sub> compound with a V<sup>+3.75</sup> valence state which had working potentials at ~4.1 V and ~2.4 V (vs Li<sup>+</sup>/Li). Boivin et al.<sup>13</sup> worked on synthesizing a larger composition range of LiVPO<sub>4</sub>O<sub>1-x</sub>F<sub>x</sub> with a mixed V<sup>+3</sup>–V<sup>+4</sup> valence state. They showed that the electrochemical performance of these materials can be tuned by changing the amount of vanadyl-type defects, i.e., the ionicity (V<sup>3+</sup>–F) or covalency (V<sup>4+</sup>=O) of the bond. All of these studies have concentrated on the compounds with LiVPO<sub>4</sub>F-type structure. However, despite the higher LiVPO<sub>4</sub>F operating potential, the V<sup>+4</sup>/V<sup>+5</sup> redox couple cannot be realized in this structure.

Due to poor diffusion kinetics and the distorted lattice of LiVPO<sub>4</sub>O, a complete lithium extraction is nearly never realized in this material. In addition, it has a poor electronic conductivity that limits its application. Improvements may be realized by changing the synthesis parameters, nanosizing, and carbon coating, which can have an effect on shortening the conduction length (Li diffusion pathway) and conductivity.<sup>10,18–23</sup> However, there has been no study on modifying the electrochemical characteristics by tuning the crystal structure of LiVPO<sub>4</sub>O. The above arguments lead to the hypothesis that a higher operating potential for V<sup>+4</sup>/V<sup>+5</sup> in LiVPO<sub>4</sub>O can be expected upon the F incorporation. In this work, our goal was to synthesize and explore structural, chemical, and electrochemical properties of the F-incorporated LiVPO<sub>4</sub>O material. A high temperature ceramic synthesis route was applied, during which LiVPO<sub>4</sub>O was incorporated with LiF. This synthesis method gave way to a direct comparison of fluorinated versus nonfluorinated LiVPO<sub>4</sub>O. The temperature dependent fluorination was subjected to a systematic characterization of the synthesis products at both the micro- and the nanoscale. This allowed insights on the effect of F on the characteristics of the LiVPO<sub>4</sub>O material and described both as general material properties and also as local changes within the material. The results showed the importance of multilevel characterization, since the average properties through larger-size samples could not always be representative for the local variations. The fluorinated counterpart was isostructural with the LiVPO<sub>4</sub>O precursor; however, local deviations from the refined structure were detected. The average valence state changed upon fluorination, but it was not homogeneous among the studied particles. The vanadium oxy/fluoro-phosphate sample clearly exhibited improved electrochemical properties compared to the nonfluorinated counterpart.

## 2. EXPERIMENTAL SECTION

**Synthesis.** Vanadium oxy/fluoro-phosphate was synthesized via two-step synthesis. In the first step, LiVPO<sub>4</sub>O precursor compound (LVPO) was synthesized through a solid-state synthesis method.<sup>24</sup> Stoichiometric amounts of V<sub>2</sub>O<sub>3</sub> vanadium(III) oxide, NH<sub>4</sub>H<sub>2</sub>PO<sub>4</sub> ammonium phosphate monobasic, and Li<sub>3</sub>PO<sub>4</sub> lithium phosphate were mixed in a planetary ball milling machine for 12 h at 600 rpm, and then the mixture was pressed as pellets. A thermal treatment was performed at 300 °C for the duration of 8 h under argon flow in order to remove ammonia.<sup>25</sup> After the heat treatment, pellets were ground to obtain a homogenized powder, which was then heated at 700 °C

for 12 h under air to obtain LVPO. In the second step, stoichiometric amounts of the as-synthesized LVPO powder were mixed and ground together with LiF and pressed as pellets with the typical weight of 150–200 mg. The pellets were subsequently introduced into a golden tube inside a special stainless steel reactor with ~2.5 mL inner volume, which was sealed inside an argon-filled glovebox. The heat treatments were carried out at various temperatures of 600 °C (LVPOF-600), 700 °C (LVPOF-700), and 800 °C (LVPOF-800) for 1 h, and then the reactors were immediately quenched in liquid nitrogen. Additionally, LiVPO<sub>4</sub>F (LVPF) powder was also prepared and characterized for the sake of comparison. The synthesis was carried out via a carbothermal reduction route to obtain VPO<sub>4</sub> and subsequent heat-treatment with LiF in the Ar-sealed stainless steel reactors, according to the method described elsewhere.<sup>8</sup> XRD analysis was used to index the peaks of the synthesized materials in order to determine their lattice parameters. XRD patterns were recorded using a PANalytical X'Pert PRO diffractometer equipped with an X'Celerator detector (128 channels) using energy discrimination and Cu Kα<sub>1</sub> radiation (λ = 1.5406 Å). Measurements were conducted in the 10–120° (2θ) angular range with increments of 0.008° at a constant counting time of 550 s per step.

**X-ray Absorption Spectroscopy (XAS).** Vanadium K-edge XANES spectra of vanadium (oxy/fluoro) phosphates and reference vanadium compounds with a known vanadium valence state and structure were measured at room temperature in transmission detection mode at the XAFS beamline of the ELETTRA synchrotron radiation facility in Trieste, Italy, and at P65 beamline of PETRA III, DESY, Hamburg. A Si(111) double-crystal monochromator was used at both beamlines with energy resolution of about 0.7 eV at 6 keV. Higher-order harmonics were effectively eliminated by a flat mirror at the P65 beamline and by detuning the second monochromator crystals to 60% of the rocking curve maximum at the XAFS beamline. The intensity of the monochromatic X-ray beam was measured by using three consecutive ionization detectors, filled with appropriate nitrogen and argon gas mixtures to obtain 15% absorption in the first cell and 80% in the second and third cell. All the V-containing samples including reference compounds (e.g., V<sub>2</sub>O<sub>5</sub>, VO<sub>2</sub>F) were prepared in the form of homogeneous pellets and pressed from micronized powder mixed with boron nitride powder. In all cases, the total absorption thickness of the sample was about 2 above the V K-edge. The absorption spectra were measured within the interval –250 eV to 1000 eV relative to the V K-edge. At the XAFS beamline, equidistant energy steps of 0.25 eV were used with the integration time of 2 s/step in the XANES region. At the P65 beamline, the absorption spectra were measured in continuous fast (3 min) scans and rebinned to the same energy steps in the XANES region as at XAFS beamline. Two to five repetitions of the scans were superimposed to improve the signal-to-noise ratio. The exact energy calibration was established with a simultaneous absorption measurement on a 5 μm thick V metal foil placed between the second and the third ionization chambers. The V K-edge in the V metal is at 5470.6 eV. Absolute energy reproducibility was ±0.02 eV. The analysis of XANES spectra is performed with Demeter (IFEFFIT) program package,<sup>26</sup> in combination with the FEFF6 program code<sup>27</sup> for ab initio calculation of photoelectron scattering paths.

**Nuclear Magnetic Resonance (NMR).** Solid-state <sup>31</sup>P and <sup>7</sup>Li magic-angle spinning (MAS) NMR spectra were recorded on a 600 MHz Varian NMR system, operating at the <sup>31</sup>P Larmor frequency of 242.65 MHz and <sup>7</sup>Li Larmor frequency of 232.97 MHz. A Varian 1.6 mm HXY MAS probe head at sample rotation frequency of 40 kHz was used. The <sup>31</sup>P MAS NMR spectrum of each sample was obtained as a sum of a series of spin-echo subspectra recorded at different irradiation frequencies.<sup>28</sup> The irradiation-frequency step was 160 kHz. Each subspectrum was phase corrected to zero order. Durations of the first and the second pulse in the rotation-synchronized spin-echo experiment were 1.8 and 3.6 μs, respectively, and the delay between the pulses was 25 μs (i.e., one rotation period). Repetition delay between consecutive scans varied between 120 s (for irradiation frequencies close to 0 ppm) and 1 s (for irradiation frequencies close to 600 ppm and beyond). The number of scans for each individual

spectrum was 32 (when recorded with the repetition delay of 120 s) or 2400 (when recorded with the repetition delay of 1 s). The frequency axes of the  $^{31}\text{P}$  MAS NMR spectra were reported relative to the signal of 85%  $\text{H}_3\text{PO}_4$ .  $^7\text{Li}$  MAS NMR spectra were obtained with a spin-echo sequence, in which the durations of the first and the second pulse were 1.4 and 2.8  $\mu\text{s}$ , respectively, and the delay between the pulses was 25  $\mu\text{s}$ . Repetition delay between consecutive scans was 100 s, and the number of scans was 24. The frequency axes of the  $^7\text{Li}$  MAS NMR spectra were reported relative to the signal of  $\text{Li}_2\text{SiO}_3$  (0 ppm).

**Microscopy.** A field-emission scanning electron microscope (FE-SEM, Model SUPRA 35VP, Carl Zeiss, Germany) was used to characterize the size and morphology of the powder samples.

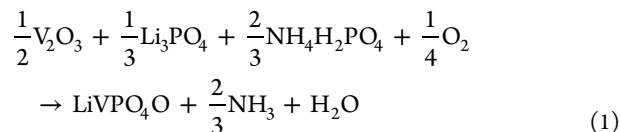
Selected area electron diffraction (SAED) was employed for the structural analysis of the synthesized materials in the transmission electron microscope (TEM). The atomic structure of synthesized materials was studied by means of high-resolution scanning TEM high-angle annular dark field (STEM-HAADF) and annular bright field (STEM-ABF) imaging. Elemental distribution was assessed by standardless energy dispersive X-ray spectroscopy in STEM mode (STEM-EDX), while the electronic structure was studied by electron energy loss spectroscopy (EELS). For these analyses, a probe aberration-corrected JEM-ARM200CF equipped with JEOL Centurio 100 mm<sup>2</sup> EDXS detector, JEOL STEM detectors (JEOL, Tokyo, Japan), and Gatan GIF Quantum ER spectrometer (Gatan, Pleasanton, U.S.A.) was employed. Specimens for electron microscopy analysis were prepared in two ways: (1) by focused ion beam (FIB) milling of a lamella from a single particle and (2) by drop casting the powder particles, which were dispersed in isopropanol on a TEM Cu grid. For FIB sample preparation, a Helios NanoLab 600i Dual-beam system (Thermo Fisher Scientific, Waltham, U.S.A., previously FEI company) was used.

**Electrode Preparation and Electrochemistry.** Cathode composites were prepared using 75 wt % of active material, 15 wt % of carbon black Printex from Degussa, and 10 wt % of PTFE as the binder. The materials were mixed by planetary ball-milling together with isopropanol at 300 rpm for 30 min, and the slurry was cast onto a carbon-coated aluminum mesh.

Circular electrodes with a diameter of 12 mm were cut out, pressed at 2 tons, and dried overnight at 80 °C. The typical loading of the active material in electrodes was  $\sim 2$  mg/cm<sup>2</sup>. The electrochemical characteristics were measured in the Swagelok cells. Two electrode cells were assembled in an argon-filled glovebox: a working electrode (WE) and a metallic Li counter electrode (CE) were placed over a separator ("Whatman" glass microfiber). The electrolyte was a 1 M solution of  $\text{LiPF}_6$  in EC:DEC in a 1:1 volume ratio (LP40, Merck). The galvanostatic measurements were performed with a rate of C/50 using a "VPM3" (Bio-Logic) potentiostat/galvanostat running with EC-Lab software.

### 3. RESULTS AND DISCUSSION

Synthesis of the LVPO ( $\text{LiVPO}_4\text{O}$ ) precursor was performed based on the eq 1:



The Fullpattern LeBail refinement matching of the XRD pattern of synthesized LVPO sample is shown in Figure S1. The photograph in the inset of Figure S1 shows the green LVPO powder. It has a triclinic crystal structure with  $\bar{P}1$  space group (space group No. 2). The structural parameters obtained through refinement are as follows:  $a$  (Å) = 6.729(1),  $b$  (Å) = 7.198(1),  $c$  (Å) = 7.928(3),  $\alpha$  (deg) = 89.812(9),  $\beta$  (deg) = 91.223(0),  $\gamma$  (deg) = 116.856(7), and  $V$  (Å<sup>3</sup>) = 342.519(2).

The as-prepared LVPO sample was mixed in a stoichiometric amount with LiF and heated at various temperatures (600, 700, and 800 °C) according to eq 2a:



The color of the powders recovered after heat treatment was brown, ranging from the light to the dark shades, with light shades corresponding to lower and dark to higher synthesis temperature. The XRD patterns of synthesized powders (LVPOF-600, LVPOF-700, and LVPOF-800) are presented in Figure 1 in selected  $2\theta$  regions chosen to emphasize the

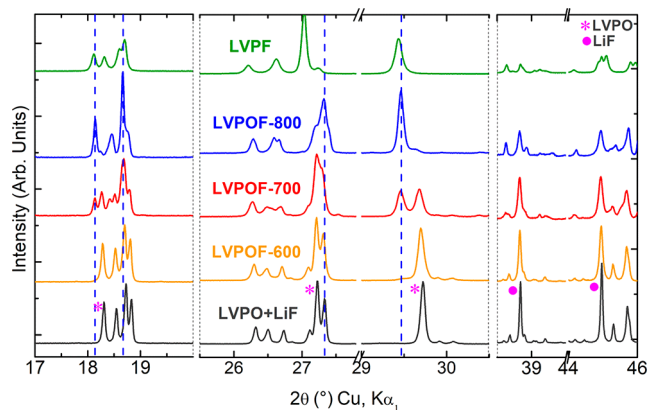


**Figure 1.** XRD patterns of LVPOF samples heat-treated at 600, 700, and 800 °C (LVPOF-600, LVPOF-700, and LVPOF-800, respectively) in a comparison with LVPO+LiF and LVPF samples. The patterns are shown in the selected  $2\theta$  regions chosen to emphasize the main peaks. Asterisks represent some of the LVPO peaks, and the circles represent LiF peaks. Blue dashed lines show the location of the LVPOF peaks.

main peaks. For the sake of comparison, XRD patterns of an unheated mixture of LVPO and LiF as well as of LVPF are shown. The continuous range ( $15^\circ$ – $60^\circ$  in  $2\theta$ ) of the X-ray diffraction patterns is presented in Figure S2. An increase in temperature from 600 to 800 °C resulted in a decrease in the intensity of LiF and LVPO peaks (marked respectively by circles and asterisks on the LVPO+LiF pattern). Simultaneously, peaks of a new phase appeared (blue vertical dashed lines), which increased in intensity from LVPOF-600 to LVPOF-800. At the highest heating temperature of 800 °C (LVPOF-800), the pattern comprises mainly of the new phase with only minor impurities in the form of LiF, LVPO, and  $\text{Li}_3\text{PO}_4$  phases. Note that the XRD pattern of the newly formed LVPOF phase is noticeably different from that of the LVPF phase (green pattern in Figure 1). The nominal composition of the expected product of complete reaction according to eq 2a was  $\text{Li}_2\text{VPO}_4\text{OF}$ . However, the presence of the LiF peaks in the XRD pattern implied an incomplete LiF consumption during the synthesis. Therefore, the amount of LiF is noted as  $x$  (with  $x < 1$ ) in eq 2b, which is a more accurate representation of the reaction that took place.



The chemical formula of the new phase (LVPOF) can be defined as  $\text{Li}_a\text{VPO}_4\text{O}_b\text{F}_c$  ( $a \geq 1$ ,  $b$ ,  $c < 1$ ). The exact amounts of the  $a$ ,  $b$ , and  $c$  values are not definite and could undergo minor variation depending on the synthesis temperature. The presence of trace impurities prevented accurate measurement or calculation of composition.

The lattice parameters of all three samples (LVPOF-600, LVPOF-700, and LVPOF-800) were refined starting from the lattice parameters of LVPO (ICSD#: 184602) using the *fullprof\_suite* program.<sup>29</sup> The refinement performed with the lattice parameters of LVPF (ICSD#: 184601) did not converge to acceptable reliability factors. The lattice parameters of LVPOF phase in each sample are reported in Table 1. The

**Table 1. Lattice Parameters of the LVPOF Phase in LVPOF-600, LVPOF-700, and LVPOF-800 Samples, Determined from LeBail Refinement**

	LVPOF-600	LVPOF-700	LVPOF-800
<i>a</i> (Å)	6.806(4)	6.809(7)	6.810(9)
<i>b</i> (Å)	7.172(9)	7.173(5)	7.182(6)
<i>c</i> (Å)	7.931(1)	7.927(9)	7.928(6)
$\alpha$ (deg)	89.96(4)	89.979(1)	89.943(7)
$\beta$ (deg)	91.454(3)	91.479(6)	91.475(9)
$\gamma$ (deg)	117.28(5)	117.21(8)	117.249(6)
<i>V</i> (Å <sup>3</sup> )	344.15(9)	344.24(6)	344.68(1)

refinement results showed that the evolution of the cell parameters does not follow a specific trend. However, the unit cell volume of the LVPOF phase in all three samples was higher than in the precursor LVPO phase. This was an expected result of the LiF incorporation into the LVPO structure. Moreover, the unit cell volume of the LVPOF phase increased with the increase of temperature from 600 to 800 °C. This indicates that, by applying higher temperature while keeping the same heat-treatment time, the incorporation of the LiF into the structure was promoted. However, further increase of the temperature resulted in melting of the LVPO and LiF mixture.

The morphology and particle size of the synthesized powders were examined by SEM. The primary particle size in the LVPO sample was in the range of 1–3  $\mu\text{m}$  on average. However, the agglomerates of up to 50  $\mu\text{m}$  in size (see Figure S3) were also detected. The particles possessed well-defined shapes. LVPOF-600 did not differ much from LVPO in size and morphology of particles. The SEM images of the LVPOF-700 sample exhibited a slightly different morphology. The particles mostly lack the defined shape seen in the precursor LVPO sample. Furthermore, the LVPOF-800 sample was constituted mainly of poorly defined particles, although larger in size (up to 10  $\mu\text{m}$ ). In general, there was a wider range of particles size in this sample (see Figure S3). It should be noted that, in the SEM images, the impurities such as LiF and Li<sub>3</sub>PO<sub>4</sub>

cannot be distinguished from the main LVPOF phase particles. In addition, LVPOF sample particles differed tremendously in size from the LVPF sample, where the average particle size was below 1  $\mu\text{m}$ . The LVPF sample particles were covered with small carbon particles which originated from the carbothermal synthesis procedure and presumably limited the particle growth during synthesis.<sup>13</sup>

Prior to the detailed analysis of the XRD patterns, XANES experiments were performed in order to assess the average oxidation state of V and its local symmetry as well as to evaluate the effects of fluorination. For that, the V K-edge XANES spectra were taken from all three LVPOF samples in addition to the LVPO and LVPF samples (Figure 2a). The shape of the edge profile and the pre-edge resonances are correlated with the local symmetry of vanadium sites, while their energy positions are correlated with the valence state of V cations.<sup>13,30–32</sup> Octahedrally coordinated vanadium cations that possess an inversion center (for example, in V<sub>2</sub>O<sub>3</sub><sup>30</sup> or LVPF<sup>12</sup>) exhibit a weak triplet resonance structure in the pre-edge region. On the other hand, vanadium cations located at sites without an inversion center (for example, tetrahedrally coordinated in CrVO<sub>4</sub>,<sup>30</sup> square pyramidal in V<sub>2</sub>O<sub>5</sub>,<sup>30</sup> or distorted octahedrally coordinated in V<sub>2</sub>O<sub>4</sub>,<sup>30</sup> Li<sub>2</sub>VTiO<sub>4</sub>,<sup>31</sup> or LVPO<sup>12</sup>) exhibit a characteristic isolated pre-edge peak. The pre-edge feature is assigned to the 1s to 3d transition, which is forbidden in a perfectly regular vanadium octahedron. This transition becomes dipole allowed with the distortion of the local symmetry around vanadium cations, which leads to 3d–4p orbital mixing. As demonstrated by Boivin et al.,<sup>13</sup> the intensity of the pre-edge peak is highly sensitive to the local distortions around vanadium in the LVPF-type LVPOF sample and gives insights into its local environments. In our case, the XANES spectra of LVPOF-600, LVPOF-700, and LVPOF-800 samples (Figure 2a) exhibited edge profiles with a pre-edge resonance. Comparison of the XANES spectra showed a gradual decrease of the prepeak intensity with increasing synthesis temperature. LVPOF-600 exhibited almost the same pre-edge peak intensity as the LVPO sample, while in LVPOF-800, the intensity of the pre-edge peak was reduced almost to half of the LVPO value. Such a decrease in the intensity of the pre-edge peak is ascribed to the increasing LVPO fluorination, which imposes higher symmetry, i.e., lower distortion in V octahedra.

In addition to the prepeak intensity, the energy shift of the vanadium absorption edge that commonly correlates with V valence was also evaluated from the XANES spectra. Generally, the increase in the V valence state is associated with the shift of

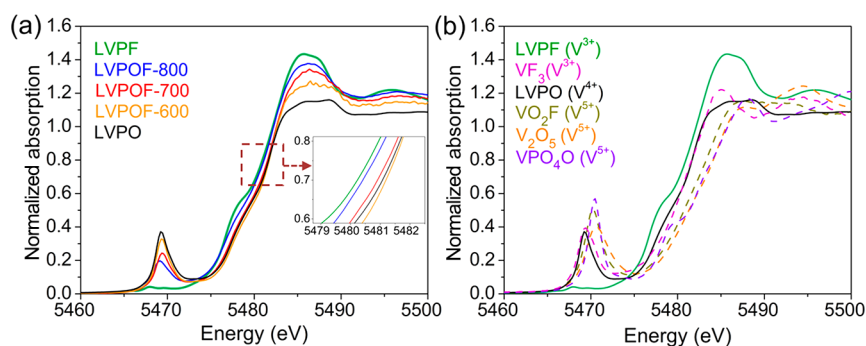


**Figure 2.** V K-edge XANES spectra of (a) LVPOF-600, LVPOF-700, and LVPOF-800 samples in a comparison to LVPO precursor and LVPF and (b) reference VO<sub>2</sub>F, V<sub>2</sub>O<sub>5</sub>, VPO<sub>4</sub>O, VF<sub>3</sub>, and LVPO and LVPF samples.

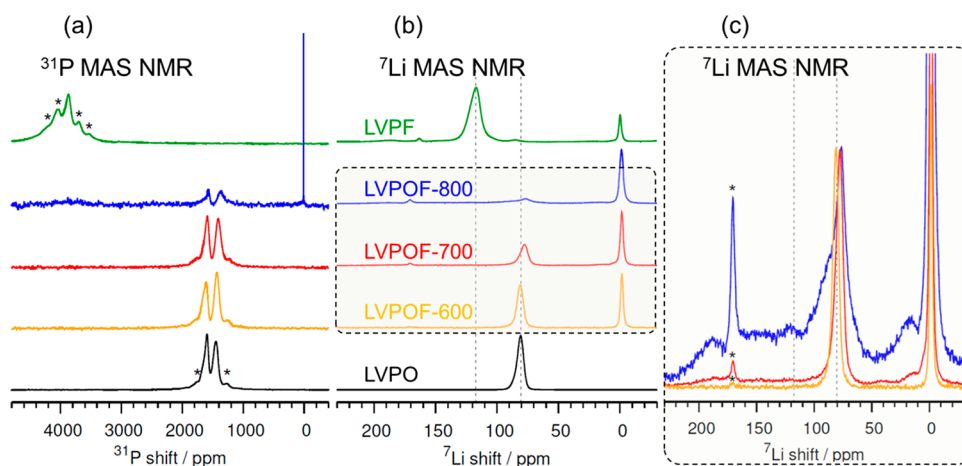


**Figure 3.**  $^{31}\text{P}$  (a) and  $^7\text{Li}$  (b) and (c) MAS NMR spectra of LVPOF-600, LVPOF-700, and LVPOF-800 samples in comparison to the LVPO precursor and LVPF. Asterisks denote spinning sidebands. In (b),  $^7\text{Li}$  NMR spectra are vertically scaled so that the highest signals of different spectra are equally high, whereas in (c) they are scaled so that the signals at ca. 80 ppm within the different spectra are equally high. Vertical dotted lines mark the positions of the  $^7\text{Li}$  resonances of LVPO and LVPF.

the edge toward higher energies, with the shift of about 2.5 eV per valence in the case of vanadium oxides.<sup>30,32</sup> The absorption edges in LVPOF-600 and LVPOF-700 were found to be very close to the energy position of the LVPO sample (see Figure 2a), while LVPOF-800 edge was shifted  $\sim 0.8$  eV to lower energies. This would imply a general trend of the reduction in the V valence state of LVPOF samples coinciding with the increase in heat treatment temperature. The LVPF sample exhibited a shift of 1 eV compared to LVPO, which correlates with a lower V valence in this structure. It should be noted, however, that the energy shifts of the absorption edge are additionally affected by the electronegativity of the ligands and the local structure of the V cations.<sup>30–32</sup>

XANES spectra of the reference samples (Figure 2b) showed that the V absorption edge position correlation in vanadium oxy/fluoro-phosphate compounds cannot be done unambiguously. The spectrum of the  $\text{VO}_2\text{F}$  ( $\text{V}^{+5}$ ) fluoride reference sample revealed the  $-0.5$  eV edge shift to the lower energies compared to the spectra of the  $\text{V}_2\text{O}_5$  ( $\text{V}^{+5}$ ) and  $\text{VPO}_4\text{O}$  ( $\text{V}^{+5}$ ) oxides due to a presence of F in the neighborhood of vanadium. Furthermore, the  $\text{VF}_3$  ( $\text{V}^{+3}$ ) edge is overlapping with the precursor LVPO ( $\text{V}^{+4}$ ), while the reference LVPF ( $\text{V}^{+3}$ ) edge is shifted about  $-0.5$  eV relative to  $\text{VF}_3$  ( $\text{V}^{+3}$ ). Therefore, the shifts in the V absorption edge position cannot be related only to the V average valence state without considering the differences in the structure and ligands (fluorination) of compared materials. The observed shifts of the vanadium edge to lower energies with increasing treatment temperature in samples LVPOF-600, LVPOF-700, and LVPOF-800 can be ascribed partially to the reduction of vanadium and partially to the effect of increased fluorination at higher temperatures.

Further, to explore the local environment of atomic species,  $^{31}\text{P}$  MAS NMR and  $^7\text{Li}$  MAS NMR spectroscopy measurements were performed. In Figure 3a,  $^{31}\text{P}$  MAS NMR spectra of LVPOF-600, LVPOF-700, and LVPOF-800 samples are compared to the spectra of the LVPO precursor and LVPF. The two signals at 1600 and 1420 ppm suggested the presence of two different types of P, which is in accordance with the two crystallographic sites observed in the pure LVPO.<sup>24</sup> This pointed out that, after the incorporation of LiF in LVPO, the host structure of LVPO was maintained. Note that both

LVPOF and LVPO phases present in the samples contributed to these signals. The  $^{31}\text{P}$  MAS NMR spectrum of the LVPOF-800 sample showed a sharp and rather intense signal at 0 ppm, corresponding to a diamagnetic impurity,  $\text{Li}_3\text{PO}_4$ , and also a very weak, broad signal at about 3900 ppm, indicating the presence of a small fraction of an LVPF-type phase.<sup>33</sup>

$^7\text{Li}$  MAS NMR spectra of the LVPOF-600, LVPOF-700, and LVPOF-800 samples showed a sharp peak at  $-2$  ppm (Figure 3b), corresponding to the remaining LiF (and of  $\text{Li}_3\text{PO}_4$  in case of LVPOF-800). All the three samples exhibited a signal at about 80 ppm, which can be assigned to Li nuclei in the LVPO type of environment. Indeed, Li atoms occupy two different crystallographic sites in LVPO, but their  $^7\text{Li}$  NMR signals cannot be resolved, because the two local environments are similar.<sup>24</sup>

A closer look at the  $^7\text{Li}$  MAS NMR spectra of LVPOF-600, LVPOF-700, and LVPOF-800 (Figure 3c) showed how LVPOF gradually transformed from a structure in which Li nuclei occupied only typical LVPO sites and exhibited an NMR signal at  $\sim 80$  ppm (LVPOF-600), to a structure in which numerous different Li environments could be found (LVPOF-800). Li nuclei experiencing these different environments gave rise to a set of strongly overlapped signals resonating between 75 and 190 ppm. Qualitatively, the  $^7\text{Li}$  MAS NMR spectrum of LVPOF-800 has similarities to the spectrum of previously reported  $\text{LiVPO}_4\text{F}_{0.25}\text{O}_{0.75}$  material.<sup>34</sup> The contribution resonating close to 120 ppm, most probably, corresponds to Li within the LVPF type of environment (this phase was already detected by  $^{31}\text{P}$  NMR). The assignment of the overlapped signals at about 75, 90, 150, and 190 ppm was not clear. Whereas signals at 84 and 186 ppm were assigned to vanadyl-type defects, the above listed various contributions to the  $^7\text{Li}$  MAS NMR spectrum of LVPOF-800 could stem from variations in Li environments. This can be small shifts of the existing positions of Li atoms due to F introduction, i.e., different distances in their neighborhood. Other possibilities include Li nuclei seeing vanadium centers in different oxidation states<sup>10</sup> and/or incorporation of additional Li atoms stemming from LiF into new sites in the  $\text{LiVPO}_4\text{O}$ -type structure. Either of these could lead to differently strong hyperfine interactions between the electronic spins of vanadium centers and lithium nuclei and thus to significant shifts of the NMR resonances.

Note that the relative intensities of the shifted signals were at least comparable to the intensities of the 80 and 120 ppm signals (corresponding to the typical LVPO and LVPOF sites, respectively), meaning that in LVPOF-800 there were significant fractions of different lithium environments.

The XRD and NMR findings showed that the crystal structure of the precursor LVPO is maintained after LiF incorporation. Therefore, the precursor LVPO and the synthesized LVPOF are isostructural. The LVPO phase crystallizes in Amblygonite type structure due to the small  $\alpha$  angle, which makes it different from the isostructural Montebasite structure ( $\alpha_{\text{Amblygonite}} < 90^\circ < \alpha_{\text{Montebasite}}$ ).<sup>35,36</sup>

The crystal structure of LVPO can be described as an arrangement of  $[\text{VO}_4\text{O}_2]$  octahedra and  $[\text{PO}_4]$  tetrahedra (Figure 4a). The octahedra are connected to each other by

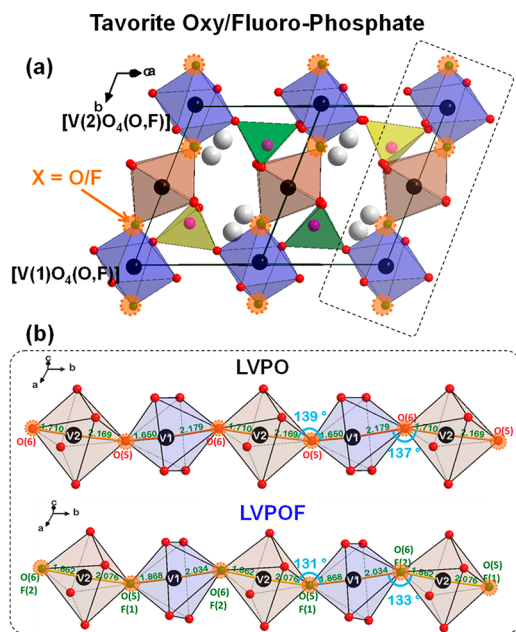


**Figure 4.** (a) Representation of the Tavorite-type structure of LVPO and LVPOF. (b) Comparison of chains of  $\cdots[\text{V}(1)\text{O}_4\text{X}_2]-[\text{V}(2)\text{O}_4\text{X}_2]\cdots$  (with  $X = \text{O}, \text{O}/\text{F}$ ) in LVPO and LVPOF.

oxygen atoms (O(5) and O(6) in Figure 4b), forming chains which run along the  $b$  direction. Along that direction, there is alternatively long ( $\text{V}-\text{O}$ ) and short ( $\text{V}=\text{O}$ ) vanadyl bonds (Figure 4b), the latter being a double bond. Within the structure, there are two types of V octahedra:  $[\text{V}(1)\text{O}_4\text{O}_2]$ , for which the equatorial plane is almost parallel to the  $b$  direction, and  $[\text{V}(2)\text{O}_4\text{O}_2]$  with the equatorial plane being almost perpendicular to the  $b$  direction. As a result, the chains are forming a *trans* arrangement along the  $b$  direction (Figure 4a). Chains of  $[\text{VO}_4\text{O}_2]-[\text{VO}_4\text{O}_2]$  are further connected to each other through  $[\text{PO}_4]$  tetrahedra. This connection is done by oxygen atoms, which are in the equatorial plane of  $[\text{VO}_4\text{O}_2]$  octahedra. There are also two types of  $[\text{PO}_4]$  tetrahedra which alternate along the  $b$  and  $a$  directions (Figure 4a). Lithium in the LVPO framework structure is located in 3D tunnels generated by polyhedra which run along the  $[110]$ ,  $[101]$ , and  $[10\bar{1}]$  directions.<sup>8,24</sup> The minimum Li-Li distance along the  $[10\bar{1}]$  tunnel in LVPO is about 5.6 Å, while in  $\text{Li}_2\text{VPO}_4\text{O}$  (with an extra incorporated Li) it is 5.3 Å in the similar  $[101]$  tunnel.<sup>10</sup> It is, thus, possible to incorporate extra Li within the

LVPO framework structure without generating steric constraints.

The atomic parameters were refined for the LVPOF-800 sample by the Rietveld method starting from the structural model of LVPO (ICSD no.: 184602) (Figure S4 and Table S1). In the LVPOF structure, one can expect the presence of randomly distributed F atoms as the ligand bridging two V octahedra along the  $b$  axis. In order to take into account the presence of fluorine in the LVPOF-800 sample, the refinement was carried out assuming F substitution (i) in either O(5) or O(6) and (ii) in both O(5) and O(6). In the first case of substitution (either O(5) or O(6)), the refinement of the XRD data delivered poor reliability factors for the minimization of the intensity difference. In the second case, where both O(5) and O(6) positions were substituted with F, the reliability factor reached satisfactory values. The best fit was achieved when the occupancy factors of O(5) and O(6) were respectively linked to F(1) and F(2). The occupancy factors for O(5), O(6), F(1), and F(2) were obtained respectively as 0.750(3), 0.846(1), 0.250(3), and 0.153(8). The substitution of F in the defined O positions of the octahedral ligands showed that  $b$  and  $c$  values in eq 2b are linked to each other in the suggested chemical notation  $(\text{Li}_a\text{VPO}_4\text{O}_b\text{F}_c)$  in the synthesis section. Thus, it is safe to reformulate the chemical notation of the LVPOF phase as  $\text{Li}_a\text{VPO}_4\text{O}_b\text{F}_{1-b}$  ( $a \geq 1, b < 1$ ), which according to the refined values can then be estimated as  $\text{Li}_a\text{VPO}_4\text{O}_{0.8}\text{F}_{0.2}$  for LVPOF-800 phase. The O and F values are calculated as the average amounts obtained for refinement of O(5), O(6), F(1), and F(2). Note that the Li position was not refined due to its low X-ray atomic scattering factor.

The V octahedral chains ( $[\text{VO}_4\text{X}_2]$  (with  $X = \text{O}$  or F ligand)) in LVPO are compared to the ones in the LVPOF phase in Figure 4b. The V1-O/F and V2-O/F long bonds in the corresponding  $[\text{V}(1)\text{O}_4\text{X}]$  and  $[\text{V}(2)\text{O}_4\text{X}]$  octahedra in LVPOF are shorter than those in LVPO, while the V1-O/F and V2-O/F short bonds are longer. This leads to a higher general symmetry of the V-X bonds in  $[\text{VO}_4\text{X}_2]$  octahedral chains of LVPOF. The higher symmetry of the V octahedra was also observed previously in XANES results as the lower pre-edge intensity in the spectrum of the LVPOF sample compared to the one for the LVPO sample. Furthermore, it can be noted from comparing the bond lengths in Figure 4b that F substitution of O has a higher impact on the elongation of a strongly covalent  $\text{V}=\text{O}$  vanadyl bond, rather than on the shortening, i.e., strengthening, of the weaker  $\text{V}-\text{O}$  bond. In addition, the V-X-V angles in LVPOF are smaller ( $131^\circ$  and  $133^\circ$ ) than the ones in LVPO ( $139^\circ$  and  $137^\circ$ ). This indicates a shrinking of the octahedral chains in the  $b$  direction in LVPOF compared to LVPO.

The crystal structure and atomic arrangements of both LVPO and LVPOF-800 were investigated by means of SAED and STEM imaging. The LVPOF-800 sample was chosen for more thorough investigations since it had the highest amount of the new LVPOF phase with the least amount of impurities. The SAED patterns collected from the single LVPOF and LVPO particles confirmed the high crystallinity of the material (Figure 5a,b). Both diffraction patterns were simulated using the JEMS software.<sup>37</sup> Corresponding structure models, i.e., ICSD no. 184602 for the LVPO and the new experimentally derived (XRD) crystallographic information file (CIF) for the LVPOF were used as the input structures. The LVPO pattern showed a good fit, while small displacements between the JEMS simulated (inset in Figure 5a) and the experimental

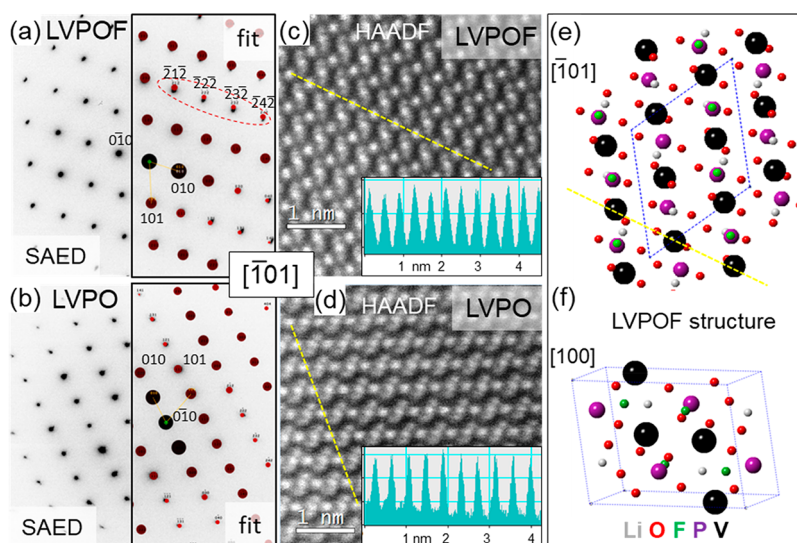


**Figure 5.** (a, c) SAED experimental patterns along with patterns simulated using *JEMS* software<sup>37</sup> for LVPOF-800 and LVPO samples, respectively. STEM-HAADF images of (b) LVPOF-800 and (d) LVPO samples, with the line intensity profiles in the insets. Yellow dashed line denotes the intensity profile position. (e) Atomic structure of the LVPOF phase viewed in the  $[\bar{1}01]$  direction along with the (f) unit cell atomic structure of the LVPOF phase pictured close to the  $[100]$  direction, with blue dashed lines denoting unit cell borders.

LVPOF pattern were detected already in the second order SAED reflections. Since the XRD pattern is collected from a millimeter-scale area of the sample, its information on the crystal structure is much less spatially resolved compared to the TEM-SAED. Therefore, the differences between the LVPOF SAED pattern and the experimental CIF file can be attributed to the nanometers-scale variations of the crystal structure due to the distribution of the O/F ligand. This goes in accordance with the previously described results of XRD, XAS, and NMR.

The STEM-HAADF images of LVPOF-800 and LVPO (Figure 5c,d, respectively) also confirmed a high crystallinity of both materials. Both images were taken in the same  $[\bar{1}01]$  zone axis but with different structure rotation (yellow dashed line in Figure 5c–e denotes the same structural plane). The contrast variations in the STEM-HAADF images correspond to the differences in the atomic numbers of the V and P (23 and 15, respectively), with the V atomic columns producing higher intensity. The model of the LVPOF atomic structure in the  $[\bar{1}01]$  zone axis is shown in Figure 5e,f. The sizes of the Li, O, F, P, and V atoms in the atomic structure drawing were normalized according to the atomic number, with V being the highest. A uniform contrast of the V and P atomic columns implies that there were no detectable defects on the V and P sublattices. The intensity line profile insets in Figure 5c,d were taken along the yellow dashed lines, which run along the plane that consists of slightly overlapping V and O atomic columns. O columns are invisible in this case due to the small distances and vicinity of the heavier V columns that produce higher intensity (Figure 5e,f). The direct visualization of the O/F ligand atomic columns was not possible neither by HAADF nor by ABF STEM imaging due to the very dense atomic packing observed in the  $[\bar{1}01]$  zone axis (Figure S6). Therefore, further STEM-EDX and STEM-EELS studies were performed to assess the local elemental composition as well as the electronic surroundings of the vanadium.

The homogeneity of the F incorporation on the nanoscale as well as overall chemical composition was studied by STEM-EDX analysis of individual particles of the LVPOF-800 sample. The STEM-EDX mapping of V, P, and O taken from a single

particle shown in Figure S6 confirmed a homogeneous distribution of these elements. Note that Li is not detectable by the EDX technique. To assess the nature of the F incorporation, i.e., whether it is homogeneously distributed throughout the particles or mainly incorporated into the particle's near-surface region (core–shell structure), the FIB lamella was cut out of the large LVPOF-800 sample particle with the diameter of  $\sim 25 \mu\text{m}$  (Figure S7). The STEM-EDX mapping performed on this FIB lamella confirmed a homogeneous incorporation of F into the large particles (Figure S8). Additionally, the STEM-EDX spectra were taken from similar thickness areas from a number of various particles, and average elemental composition was determined to be  $V = 11.7 \pm 2.6$  atom %,  $P = 15.5 \pm 1.8$  atom %,  $O = 61.8 \pm 1.5$  atom %, and  $F = 9.5 \pm 2.5$  atom %. Comparing the absolute errors ( $1\sigma$ ) given for each individual element of LVPOF-800, precursor LVPO, and reference LVPOF (see Table S2), one can see that compositional variations in all of the involved elements are highest for the LVPOF-800 sample.

The EELS measurements were used to probe the oxidation state of the vanadium atoms within various samples at the nanoscale through monitoring  $V\text{-}L_2$  and  $V\text{-}L_3$  edges (Figure 6a). The edge onset energy and  $L_3/L_2$  peaks intensity ratio (so-called white-line ratio) are related to the oxidation state of the vanadium atoms. Generally, there are two methods for determination of the elemental valence from the EEL spectrum. In the white-line ratio method, the integral intensity ratio of the  $V\text{-}L_3$  and  $V\text{-}L_2$  excitation peaks is correlated to its oxidation state. The other method involves examination of displacement of excitation energy (shift of the edge onset) or so-called chemical shift. The latter method is in general more suitable for V oxide materials due to the overlapping of  $V\text{-}L_{2,3}$  and  $O\text{-}K$  edges. However, both methods should be examined for analyzing the oxidation state and local atomic environment.<sup>38</sup> It can be seen in Figure 6a that the V edge onset undergoes a shift toward lower energies as well as a reduction in the  $L_3/L_2$  white-line ratio, from precursor LVPO through LVPOF-800 to LVPOF. This observation is in agreement with the XANES results (Figure 2), in which a shift in edge position

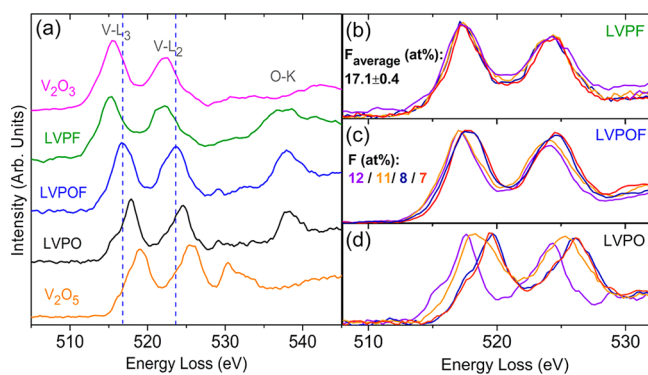


**Figure 6.** EELS spectra obtained at 80 kV electron beam energy: (a) comparison of LVPO, LVPOF-800, LVPF, and reference  $V_2O_3$  and  $V_2O_5$  samples and (b) comparison of four different particles of (b) LVPF, (c) LVPOF-800, and (d) LVPO.

toward lower energies was seen in similar order. The physical phenomena probed by the XANES and EELS techniques are of the same nature differing only in the probed area. Consequently, the shifts of the  $V-L_{2,3}$  edge position in the EEL spectra are as well due to the contributions of both varying F content and V valence changes. With the EELS analysis we could concentrate on the effect of the F amount in the LVPO-type structure.

STEM-EELS analysis, due to its nature, is performed with much higher spatial resolution than XANES, allowing the assessment of the electronic properties at the nanometer scale. The edge behavior in spectra taken from four different LVPF reference sample particles was rather stable (Figure 6b), whereas there were clear variations in edge onset positions in LVPOF-800 and LVPO particles' spectra (Figure 6c,d). The occurrence of these variations in the LVPO precursor could be attributed to the presence of the O vacancies in the lattice. Such a defective O sublattice in the precursor material could promote the F incorporation into the structure. The variations in the LVPOF-800 spectra could be ascribed to the residual O vacancies as well as to the local variations in the incorporated F content among the particles. To evaluate this, the amount of the incorporated F in the LVPOF-800 sample was correlated to the edge onset position via performing simultaneous STEM-EDX and EELS analysis. All of the measurements were carried out with similar conditions in the microscope, such as acceleration voltage, probe current, examined region of interest, and data collection time. Figure 6c shows the EEL

spectra taken from four different LVPOF-800 particles along with EDX defined F content of 7%, 8%, 11%, and 12%. Higher F amount resulted in a  $V L_{2/3}$  edge onset shift toward lower energies as well as in a decrease in  $L_{2/3}$  white-line ratio (lower valence state). This further confirmed the impact of F and its amount in the V edge shift, observed also through XANES results. The varying F amounts were indicative of a range of solid solution phases rather than a single phase at the single particle scale, which in its turn would influence the resulting electrochemical properties.

The galvanostatic charge/discharge (Li extraction/insertion) signature of LVPOF samples was investigated and compared to the LVPO precursor and LVPF by testing them as a cathode material in a half-cell battery configuration. Figure 7a compares the galvanostatic cycling curves of LVPOF-600, LVPOF-700, and LVPOF-800 samples at high-voltage domain (3.0–4.5 V vs  $Li^+/Li$ ) with a current density corresponding roughly to C/50 cycling rate. The electrochemical signature of LVPOF-600 was similar to that of the LVPO phase (Figure 7b): a biphasic reaction at  $\sim 3.95$  V involving  $V^{4+}/V^{5+}$  redox couple. The same redox couple can be encountered in the LVPOF-700 sample. However, here the LVPO phase contributed to only about half of the overall capacity. The other half, therefore, can be attributed to the new LVPOF phase with a higher potential of 4.18 V. LVPOF-800 was mainly composed of the LVPOF phase contributing to the electrochemical performance, although an insignificant feature of the LVPO phase can still be seen. Lithium extraction/insertion proceeded through a sloping voltage profile which could be an indication of a solid solution-like mechanism. The appearance of such solid solution-like behavior can originate from the presence of the defects detected by EELS analysis. The literature reports that in the case of the defect-free  $LiFePO_4$  material, a biphasic mechanism (well-defined plateau) takes place, whereas for the defective  $LiFePO_4$ , a sloping curve characteristic of a solid-solution mechanism occurs.<sup>39,40</sup>

The low specific capacity observed for LVPOF-600 and LVPOF-700 (Figure 7a) are correlated to the large amount of LVPO phase present in both samples, which has been reported to present a poor charge/discharge capacity.<sup>10,24</sup> Figure 7b shows the galvanostatic cycling curves of LVPO, LVPOF-800, and LVPF obtained at the high-voltage domain. The extraction/insertion of Li in LVPOF-800 took place at around 4.12 V vs  $Li^+/Li$  (for mixed  $V^{3+}/V^{4+}$  and  $V^{4+}/V^{5+}$  redox couples), which differed from LVPO (3.95 V for  $V^{4+}/V^{5+}$  redox couple) and LVPF (4.26 V for  $V^{3+}/V^{4+}$  redox couple). An

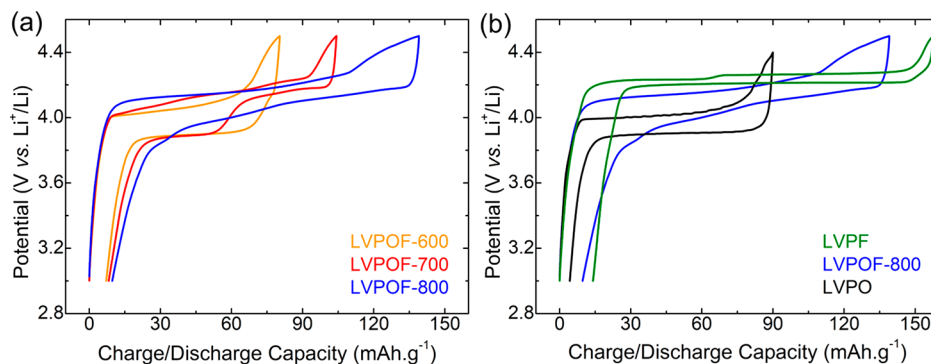


**Figure 7.** Galvanostatic cycling curves obtained vs Li at a C/50 rate for (a) LVPOF-600, LVPOF-700, and LVPOF-800 samples and (b) LVPO, LVPOF-800, and LVPF, in the high-voltage domain (i.e., between 3.0 and 4.5 V vs  $Li^+/Li$ ).

increment of the working potential in LVPOF-800 with respect to the precursor LVPO was expected due to the inductive effect of the incorporated F, which would increase the ionic character of V–O/F with respect to V–O bonds in LVPO. In addition, LVPOF showed higher charge/discharge capacity compared to LVPO. We believe that F incorporation can improve the low kinetics of Li diffusion in LVPO structure and therefore allow for a higher Li exchange during electrochemical cycling. The polarization of the LVPOF-600 followed the pattern observed in the LVPO sample (Figure 7b). In the LVPOF-700, the polarization changes were due to the presence of two phases, LVPO and LVPOF. Polarization of the LVPOF phase in the LVPOF-700 sample was much lower than that of LVPO. This enhancement can be partly related to the mixed valence state,  $V^{3+}/V^{4+}$ , which is a result of fluorine substitution in V–O ligands of  $[VO_6]$  octahedral chains. The higher charge transfer and enhanced hopping process between  $V^{3+}$  and  $V^{4+}$  cations in LVPOF could lead to higher conductivity and, thus, lower polarization.<sup>12,41</sup> However, the polarization of the LVPOF phase here differed from that observed in the LVPOF-800 sample, where LVPOF was the main contributing phase. The reason for that can be the particle size difference between the two samples.

The galvanostatic cycling curves of LVPOF-600, LVPOF-700, and LVPOF-800 samples at low-voltage domain (i.e., between 1.5 and 3 V vs  $Li^+/Li$ ) are shown in Figure S9. LVPOF-600 showed similar electrochemical signature as LVPO,<sup>8</sup> also for the insertion reaction of Li into the structure. This reaction proceeded through a series of phase transitions at 2.47, 2.21, and 2.03 V vs  $Li^+/Li$  involving the  $V^{IV}/V^{III}$  redox couple, which would lead to formation of  $Li_2VPO_4O$ . This behavior was also observed for LVPOF-700; however, an additional plateau appeared at  $\sim 1.78$  V. The specific capacity of LVPOF-700 for the insertion of Li is almost half of the one for LVPOF-600. The reduction of specific capacity is linked to the presence of the LVPOF phase, since LVPOF-800 showed an even lower Li insertion capacity during a sloping voltage cycling curve. This curve resembles the cycling signature of LVPO, even though it lacks the biphasic steps, and this can be another indication of LVPO-type structure. The low activity of the LVPOF phase, which led to low specific capacity, can be attributed to the extra Li in the  $Li_aVPO_4O_bF_{1-b}$  compound. It is presumed that the extra Li ions occupy the available Li sites and only a limited amount of additional Li ions can be inserted.

#### 4. CONCLUSION

We have, to the best of our knowledge, for the first time synthesized a  $LiVPO_4O$ -type oxy/fluoro-phosphate phase. In the synthesis procedure, the  $LiVPO_4O$  precursor compound was fluorinated via LiF incorporation during a high-temperature ceramic synthesis. The new phase contains mixed O/F ligand atoms bridging the octahedra chains. The formation of ionic V–F bonds in LVPOF increased the redox potential compared to V–O and highly covalent V=O bonds in LVPO. The LVPOF phase was confirmed to be isostructural with the precursor LVPO; however, local deviations from the refined LVPOF structure were detected. The distortion of V octahedra in the precursor LVPO structure was reduced through the F incorporation. The average V valence in LVPOF was reduced compared to the precursor LVPO. The amount of incorporated F varied among particles, which indicated the formation of a solid solution phase. This gave rise to the observed local

fluctuations of the V oxidation state among different particles. The vanadium valence variations within the precursor LVPO sample particles were found to be partially compensated in the vanadium oxy/fluoro-phosphate structure. However, due to the nature of the vanadium oxide containing compounds as well as the unclear impact of the F substitution in O sublattice on spectral features, the exact valence value could not be determined unambiguously. The operating potential of the new LVPOF phase is increased compared to that of the precursor LVPO (4.12 V vs 3.95 V vs metallic lithium, respectively) but still lower compared to LVPF phase. We have clearly shown that it is possible to achieve an LVPO-type structure for the LVPOF compound by the proposed synthesis method. On a broader scale, our results demonstrate that enhancement of the electrochemical characteristics is possible by introduction of a mixed ligand into the initial Favortite structure. However, the exact nature of the redox couple in the new LVPOF compound remains debatable.

#### ■ ASSOCIATED CONTENT

##### Supporting Information

The Supporting Information is available free of charge at <https://pubs.acs.org/doi/10.1021/acs.chemmater.9b03698>.

XRD refined patterns, SEM images, STEM-HAADF, STEM-ABF images, EDX maps, tables of atomic parameters, and EDX chemical composition (PDF)

#### ■ AUTHOR INFORMATION

##### ORCID

Gregor Mali: 0000-0002-9012-2495

Gregor Kapun: 0000-0003-0007-4678

Robert Dominko: 0000-0002-6673-4459

##### Notes

The authors declare no competing financial interest.

#### ■ ACKNOWLEDGMENTS

This research was supported by the project LiRichFCC under the Grant Agreement No. 711792 from the EU Horizon 2020 research and innovation programme, by the Slovenian Research Agency (core research programs P1-0112 and P2-0393 and P1-0021), and by the project CALIPSOplus under the Grant Agreement 730872 from the EU Framework Programme for Research and Innovation HORIZON 2020. We acknowledge the financial support from the TUBITAK – ARRS Program Code 2508, Project No. 112M018, which initiated the collaboration between National Institute of Chemistry, Slovenia, and Sabanci University, Turkey. We also acknowledge the access to the SR facilities of ELETTRA (beamline XAFS, pr. 20175158) and DESY, Hamburg, Germany, a member of the Helmholtz Association (beamline P65, pr. I-20170691 EC). We would like to thank Simone Pollastri, Mateusz Czyzycki, Giuliana Aquilanti, and Luca Olivi of ELETTRA and Edmund Welter, Ruidy Nemausat, and Mathias Herrmann from P65 beamline of DESY for assistance during the experiment and expert advice on beamline operation.

#### ■ REFERENCES

(1) Masquelier, C.; Croguennec, L. Polyanionic (Phosphates, Silicates, Sulfates) Frameworks as Electrode Materials for Rechargeable Li (or Na) Batteries. *Chem. Rev.* **2013**, *113* (8), 6552–6591.

- (2) Whittingham, M. S. Ultimate limits to intercalation reactions for lithium batteries. *Chem. Rev.* **2014**, *114* (23), 11414–11443.
- (3) Antipov, E. V.; Khasanova, N. R.; Fedotov, S. S. Perspectives on Li and transition metal fluoride phosphates as cathode materials for a new generation of Li-ion batteries. *IUCrJ* **2015**, *2* (1), 85–94.
- (4) Julien, C.; Mauger, A.; Vijh, A.; Zaghbi, K. Polyanionic compounds as cathode materials. In *Lithium Batteries*; Springer: 2016; pp 201–267.
- (5) Azmi, B. M.; Ishihara, T.; Nishiguchi, H.; Takita, Y. LiVPO<sub>4</sub> as a new cathode materials for Li-ion rechargeable battery. *J. Power Sources* **2005**, *146* (1–2), 525–528.
- (6) Barker, J.; Gover, R.; Burns, P.; Bryan, A.; Saidi, M.; Swoyer, J. Structural and electrochemical properties of lithium vanadium fluorophosphate, LiVPO<sub>4</sub>F. *J. Power Sources* **2005**, *146* (1–2), 516–520.
- (7) Barker, J.; Gover, R.; Burns, P.; Bryan, A. A symmetrical lithium-ion cell based on lithium vanadium fluorophosphate, LiVPO<sub>4</sub>F. *Electrochem. Solid-State Lett.* **2005**, *8* (6), A285–A287.
- (8) Ateba Mba, J.-M.; Masquelier, C.; Suard, E.; Croguennec, L. Synthesis and Crystallographic Study of Homeotypic LiVPO<sub>4</sub>F and LiVPO<sub>4</sub>O. *Chem. Mater.* **2012**, *24* (6), 1223–1234.
- (9) Ateba Mba, J.-M.; Croguennec, L.; Basir, N. I.; Barker, J.; Masquelier, C. Lithium insertion or extraction from/into tavorite-type LiVPO<sub>4</sub>F: an in situ X-ray diffraction study. *J. Electrochem. Soc.* **2012**, *159* (8), A1171–A1175.
- (10) Bianchini, M.; Ateba-Mba, J. M.; Dagault, P.; Bogdan, E.; Carlier, D.; Suard, E.; Masquelier, C.; Croguennec, L. Multiple phases in the  $\epsilon$ -VPO<sub>4</sub>O–LiVPO<sub>4</sub>O–Li<sub>2</sub>VPO<sub>4</sub>O system: a combined solid state electrochemistry and diffraction structural study. *J. Mater. Chem. A* **2014**, *2* (26), 10182–10192.
- (11) Julien, C.; Mauger, A.; Vijh, A.; Zaghbi, K. Fluoro-polyanionic Compounds. In *Lithium Batteries*; Springer: 2016; pp 269–293.
- (12) Kim, M.; Lee, S.; Kang, B. High Energy Density Polyanion Electrode Material: LiVPO<sub>4</sub>O<sub>1-x</sub>F<sub>x</sub> ( $x \approx 0.25$ ) with Tavorite Structure. *Chem. Mater.* **2017**, *29* (11), 4690–4699.
- (13) Boivin, E.; David, R.; Chotard, J.-N.; Bamine, T.; Iadecola, A.; Bourgeois, L.; Suard, E.; Fauth, F.; Carlier, D.; Masquelier, C.; Croguennec, L. LiVPO<sub>4</sub>F<sub>1-y</sub>O<sub>y</sub> Tavorite-Type Compositions: Influence of the Concentration of Vanadyl-Type Defects on the Structure and Electrochemical Performance. *Chem. Mater.* **2018**, *30* (16), 5682–5693.
- (14) Boivin, E.; Chotard, J.-N. I.; Ménétrier, M.; Bourgeois, L.; Bamine, T.; Carlier, D.; Fauth, F. o.; Masquelier, C.; Croguennec, L. Oxidation under air of tavorite LiVPO<sub>4</sub>F: influence of vanadyl-type defects on its electrochemical properties. *J. Phys. Chem. C* **2016**, *120* (46), 26187–26198.
- (15) Boivin, E.; Iadecola, A.; Fauth, F.; Chotard, J.-N.; Masquelier, C.; Croguennec, L. The redox paradox of Vanadium in Tavorite LiVPO<sub>4</sub>F<sub>1-y</sub>O<sub>y</sub>. *Chem. Mater.* **2019**, *31* (18), 7367–7376.
- (16) Onoda, M.; Ishibashi, T. Phase Transition and Spin Dynamics of the LiVPO<sub>4</sub> Insertion Electrode with the S= 1 Linear Chain and the Development of F–O Mixed System. *J. Phys. Soc. Jpn.* **2015**, *84* (4), No. 044802.
- (17) Ma, R.; Shao, L.; Wu, K.; Shui, M.; Wang, D.; Long, N.; Ren, Y.; Shu, J. Effects of oxidation on structure and performance of LiVPO<sub>4</sub>F as cathode material for lithium-ion batteries. *J. Power Sources* **2014**, *248*, 874–885.
- (18) Harrison, K. L.; Manthiram, A. Microwave-assisted solvothermal synthesis and characterization of various polymorphs of LiVPO<sub>4</sub>. *Chem. Mater.* **2013**, *25* (9), 1751–1760.
- (19) Ren, M.; Zhou, Z.; Gao, X.; Liu, L.; Peng, W. LiVPO<sub>4</sub> hollow microspheres: one-pot hydrothermal synthesis with reactants as self-sacrifice templates and lithium intercalation performances. *J. Phys. Chem. C* **2008**, *112* (33), 13043–13046.
- (20) Shi, Y.; Zhou, H.; Seymour, I. D.; Britto, S.; Rana, J.; Wangoh, L. W.; Huang, Y.; Yin, Q.; Reeves, P. J.; Zuba, M.; et al. Electrochemical Performance of Nanosized Disordered LiVPO<sub>4</sub>. *ACS Omega* **2018**, *3* (7), 7310–7323.
- (21) Shi, Y.; Zhou, H.; Britto, S.; Seymour, I. D.; Wiaderek, K. M.; Omenya, F.; Chernova, N. A.; Chapman, K. W.; Grey, C. P.; Whittingham, M. S. A high-performance solid-state synthesized LiVPO<sub>4</sub> for lithium-ion batteries. *Electrochem. Commun.* **2019**, *105*, 106491.
- (22) Zhou, H.; Shi, Y.; Xin, F.; Omenya, F.; Whittingham, M. S.  $\epsilon$ - and  $\beta$ -LiVPO<sub>4</sub>: Phase Transformation and Electrochemistry. *ACS Appl. Mater. Interfaces* **2017**, *9* (34), 28537–28541.
- (23) Saravanan, K.; Lee, H. S.; Kuezma, M.; Vittal, J. J.; Balaya, P. Hollow  $\alpha$ -LiVPO<sub>4</sub> sphere cathodes for high energy Li-ion battery application. *J. Mater. Chem.* **2011**, *21* (27), 10042–10050.
- (24) Ateba Mba, J.-M. New Lithium Transition Metal Fluorophosphates as Positive Electrode Materials for Li-ion Batteries. PhD thesis, Bordeaux University, Bordeaux, 2013.
- (25) Viswanath, R. S.; Miller, P. J. High Temperature Phase Transition ni NH<sub>4</sub>H<sub>2</sub>PO<sub>4</sub>. *Solid State Commun.* **1979**, *32* (8), 703–706.
- (26) Ravel, B.; Newville, M. ATHENA, ARTEMIS, HEPHAESTUS: data analysis for X-ray absorption spectroscopy using IFEFFIT. *J. Synchrotron Radiat.* **2005**, *12* (4), 537–541.
- (27) Rehr, J.; Albers, R.; Zabinsky, S. High-order multiple-scattering calculations of X-ray-absorption fine structure. *Phys. Rev. Lett.* **1992**, *69* (23), 3397.
- (28) Pell, A. J.; Clément, R. J.; Grey, C. P.; Emsley, L.; Pintacuda, G. Frequency-stepped acquisition in nuclear magnetic resonance spectroscopy under magic angle spinning. *J. Chem. Phys.* **2013**, *138* (11), 114201.
- (29) Rodriguez-Carvajal, J. FULLPROF: a program for Rietveld refinement and pattern matching analysis. Presented at the satellite meeting on powder diffraction of the XV congress of the IUCr, Toulouse, France, 1990.
- (30) Wong, J.; Lytle, F.; Messmer, R.; Maylotte, D. K-edge absorption spectra of selected vanadium compounds. *Phys. Rev. B: Condens. Matter Mater. Phys.* **1984**, *30* (10), 5596.
- (31) Dominko, R.; Garrido, C. V.-A.; Bele, M.; Kuezma, M.; Arcon, I.; Gaberscek, M. Electrochemical characteristics of Li<sub>2-x</sub>VTiO<sub>4</sub> rock salt phase in Li-ion batteries. *J. Power Sources* **2011**, *196* (16), 6856–6862.
- (32) Pivko, M.; Arcon, I.; Bele, M.; Dominko, R.; Gaberscek, M. A<sub>3</sub>V<sub>2</sub>(PO<sub>4</sub>)<sub>3</sub> (A= Na or Li) probed by in situ X-ray absorption spectroscopy. *J. Power Sources* **2012**, *216*, 145–151.
- (33) Messinger, R. J.; Ménétrier, M.; Salager, E.; Boulineau, A.; Duttine, M.; Carlier, D.; Ateba Mba, J.-M.; Croguennec, L.; Masquelier, C.; Massiot, D.; Deschamps, M. Revealing Defects in Crystalline Lithium-Ion Battery Electrodes by Solid-State NMR: Applications to LiVPO<sub>4</sub>F. *Chem. Mater.* **2015**, *27* (15), 5212–5221.
- (34) Boivin, É. Crystal chemistry of vanadium phosphates as positive electrode materials for Li-ion and Na-ion batteries. Ph.D. thesis, University of Picardie Jules Verne, Amiens, 2017.
- (35) Groat, L. A.; Raudsepp, M.; Hawthorne, F. C.; Ercit, T. S.; Sherriff, B. L.; Hartman, J. S. The amblygonite-montebbrasite series; characterization by single-crystal structure refinement, infrared spectroscopy, and multinuclear MAS-NMR spectroscopy. *Am. Mineral.* **1990**, *75* (9–10), 992–1008.
- (36) Groat, L. A.; Chakoumakos, B. C.; Brouwer, D. H.; Hoffman, C. M.; Fyfe, C. A.; Morell, H.; Schultz, A. J. The amblygonite (LiAlPO<sub>4</sub>F)-montebbrasite (LiAlPO<sub>4</sub>OH) solid solution: A combined powder and single-crystal neutron diffraction and solid-state 6Li MAS, CP MAS, and REDOR NMR study. *Am. Mineral.* **2003**, *88* (1), 195–210.
- (37) Stadelmann, P. *Electron Microscopy Software-Java Version (JEMS)*; CIME–EPFL: Lausanne, Switzerland, 1999, 2011.
- (38) Tan, H.; Verbeeck, J.; Abakumov, A.; Van Tendeloo, G. Oxidation state and chemical shift investigation in transition metal oxides by EELS. *Ultramicroscopy* **2012**, *116*, 24–33.
- (39) Gibot, P.; Casas-Cabanas, M.; Laffont, L.; Levasseur, S.; Carlach, P.; Hamelet, S.; Tarascon, J.-M.; Masquelier, C. Room-temperature single-phase Li insertion/extraction in nanoscale Li<sub>x</sub>FePO<sub>4</sub>. *Nat. Mater.* **2008**, *7*, 741.

- (40) Mestre-Aizpurua, F.; Hamelet, S.; Masquelier, C.; Palacin, M. High temperature electrochemical performance of nanosized LiFe-PO<sub>4</sub>. *J. Power Sources* **2010**, *195* (19), 6897–6901.
- (41) Chung, S.-Y.; Bloking, J. T.; Chiang, Y.-M. Electronically conductive phospho-olivines as lithium storage electrodes. *Nat. Mater.* **2002**, *1* (2), 123.